Kinetics of the low-pressure chemical vapor deposited tungsten nitride process using tungsten hexafluoride and ammonia precursors

Downloaded from: https://research.chalmers.se, 2026-10-11 17:42 UTC

Citation for the original published paper (version of record):
Gerdin Hulkko, J., Böőr, K., Qiu, R. et al (2021). Kinetics of the low-pressure chemical vapor deposited tungsten nitride process using tungsten hexafluoride and ammonia precursors. Journal of Vacuum Science and Technology A, 39(6): 063403-. http://dx.doi.org/10.1116/6.0001093

N.B. When citing this work, cite the original published paper.

research.chalmers.se offers the possibility of retrieving research publications produced at Chalmers University of Technology. It covers all kind of research output: articles, dissertations, conference papers, reports etc. since 2004. research.chalmers.se is administrated and maintained by Chalmers Library

(article starts on next page)

JVST A
Journal of Vacuum Science & Technology A

ARTICLE

avs.scitation.org/journal/jva

Kinetics of the low-pressure chemical vapor deposited tungsten nitride process using tungsten hexafluoride and ammonia precursors

Cite as: J. Vac. Sci. Technol. A 39, 063403 (2021); doi: 10.1116/6.0001093
Submitted: 21 April 2021 · Accepted: 17 August 2021 ·
Published Online: 17 September 2021

View Online Export Citation CrossMark

Johan G. Hulkko,[1,a)] Katalin Böőr,[1] Ren Qiu,[2] Olof Bäcke,[2] Mats Boman,[1] Mats Halvarsson,[2] and Erik Lindahl[3]

AFFILIATIONS

[1]Department of Chemistry–Ångström Laboratory, Uppsala University, 75120 Uppsala, Sweden
[2]Department of Physics, Chalmers University of Technology, 41296 Gothenburg, Sweden
[3]AB Sandvik Coromant, 12679 Hägersten, Sweden

[a)]**Electronic mail:** johan.gerdin@kemi.uu.se

ABSTRACT

Tungsten nitride (WN_x) is a hard refractory material with low electrical resistance that can be deposited using multiple methods. This study focuses on the microstructrual development of low pressure chemical vapor deposition grown WN_x coatings. Also, the growth kinetics is studied and discussed in terms of the resulting microstructures. Samples of WN_x were deposited using WF_6, NH_3, and Ar at 592–887 K in a hot-wall reactor with variable gas mixture compositions (NH_3:WF_6 = 0.5–25). The coatings were nitrogen-rich ($x \sim 1.65$) and oxygen-free as determined by time-of-flight-elastic recoil detection analysis. X-ray diffraction showed that the coatings transformed from being amorphous to crystallizing as β-W_2N at 641–690 K. The morphologies changed with deposition temperature. Being very fine grained and nodular at deposition temperatures 740 K and below, increasing the deposition temperature to 789 K while employing a NH_3:WF_6 molar ratio of 1, large disc-shaped protrusions were formed. When increasing the NH_3:WF_6 molar ratio to 25, striped facets became increasingly dominant. Investigating the latter by transmission electron microscopy, a microstructure of smaller ridges formed by twinning, oriented as <211> in the out-of-plane direction, was revealed across the facet surfaces. Transmission Kikuchi diffraction confirmed that <211> was the texture of these coatings. The partial reaction order of WF_6 and NH_3 at 740 K was determined to be close to 1/6 and 1/2, respectively. The apparent activation energy ranged from 82 to 12 kJ/mol corresponding to deposition temperatures from 592 to 887 K.

© 2021 Author(s). All article content, except where otherwise noted, is licensed under a Creative Commons Attribution (CC BY) license (http://creativecommons.org/licenses/by/4.0/). https://doi.org/10.1116/6.0001093

I. INTRODUCTION

One of the objectives for the development of chemical vapor deposition (CVD) coatings, and later atomic layer deposition (ALD), of W and WN_x, was the need for new contact materials in electronics in the 1980s. Complex electronic architectures provide challenges that for which CVD is well suited. CVD coatings can achieve a high material density that is important in order to obtain a high conductivity. Also, having gaseous reactants and by-products operated at lower pressure means that deep vias, which are needed for making interconnects, or otherwise complex geometry can be deposited uniformly. This is something that some other techniques, such as physical vapor deposition (PVD), struggle with.

The formation of CVD-W using hydrogen has previously been studied on blanket layers and plug-fills in electrical contacts. To enhance the reactivity, a catalyst, such as silane (SiH_4),[1–3] disilane (Si_2H_4),[4] or diborane (B_2H_6),[5,6] is commonly introduced. CVD-W has high conductivity and can be selectively deposited on exposed Si on masked, oxidized surfaces. Apart from electronic applications, tungsten can also act as a screening material of radiation from radioactive sources.

CVD-WN_x has low electrical resistivity and constitutes an effective diffusion barrier between various materials, such as copper and silicon. LPCVD-WN_x coatings were demonstrated in the late 1980s by Nakajima *et al.*[7] using a mixture of WF_6, NH_3, and H_2 in a hot-wall reactor. The total LPCVD reaction of the nitride reaction

© Author(s) 2021

was described as

$$2WF_6(g) + xNH_3(g) + (6 - 3/2x)H_2 \rightarrow W(s) + 12HF + 1/2(x-1)N_2(g), \quad (1)$$

where $x = 1$–4. The reaction is complex, and side reactions are known to take place. One of them is the decomposition of ammonia, which is catalyzed by metallic surfaces. According to Frankenburger and Holder,[8] the release of $H_2(g)$ from this decomposition is relatively fast, particularly, on tungsten surfaces. In this case, the various nitrogen species remain on the surface longer in the form of ammonia, imide, or tungsten nitride. The produced H^* and $H_2(g)$ can take part in other reactions, for instance, the reduction of WF_x either on the surface or in the gas phase

$$2WF_x(g) + 2H_2(g)2WF_{(x-1)}(g) + 2HF(g) + H_2(g), \quad (2)$$

$$WF_6(g) + 3H_2(g)W(s) + 6HF(g), \quad (3)$$

where ($x = 1$–6). A second reaction to be considered is the homogeneous formation of ammonium complexes, such as ammonium fluorides, $NH_3{\cdot}(HF)_2$ ($T_{sub} < 100$ °C)[9] and $NH_3{\cdot}(HF)$[2] ($T_{bp} = 240$ °C),[10] as well as adducts with tungsten fluoride, such as $WF_5{\cdot}NH_2$ (Ref. 2) and $WF_6{\cdot}(NH_3)_4$ (Refs. 6 and 11) that occur at lower deposition temperatures. These by-products can condensate on the surface where they may block active surface sites and introduce impurities. However, at CVD temperatures above 550 K in a hot-wall reactor, this should not be a problem with regard to ammonium fluoride. In the gas phase, these adducts could deplete the gas supply if unreactive but could also serve as a step in the deposition process.

The properties of a thin film depend on the microstructure, morphology, coating, and phase composition. In turn, those properties are the result of the growth mode that is determined by, for instance, the reactor temperature, the partial pressure of precursors and also possible substrate interactions. While the LPCVD-WN_x process has been studied extensively, most studies have focused on electronic properties. Physical properties such as hardness and Young's modulus are rarely reported for CVD-WN_x coatings. In applications where several material layers are deposited in sequence, the morphology of the interface between the materials is of great importance to not only conductivity but also tribology as it determines adhesion and can act as a source of crack formation.

The aim of this study is to understand the growth behavior in the hot-wall LPCVD-WN_x process using WF_6, NH_3, and Ar. In particular, the kinetics, microstructure, and texture are investigated. Kinetics is important to the development of the microstructure and texture. The deposition rate and growth mode determine if vacancies and other structural defects can be introduced, which is possible during mass transport control. Otherwise, the growth is governed by surface kinetics which can allow for better texture control due to the slower overall reaction rate. α-Al_2O_3 (000l) substrates were used to minimize potential chemical substrate-coating interactions. The coating morphology and microstructures were characterized using electron microscopy. Phase and elemental compositions were investigated by a combination of x-ray diffraction (XRD) and time of flight–elastic recoil detection analysis (TOF-ERDA). The relative coating thickness was estimated using x-ray fluorescence (XRF) spectroscopy.

II. EXPERIMENTAL SETUP AND METHODOLOGY

The samples were deposited by CVD in a horizontal tube hot-wall reactor. The reactor has been described previously and has been equipped with a custom gas distribution device produced in 316 l by additive manufacturing.[12] The device, similar to a conventional shower head but designed for horizontal distribution, was positioned upstream at the start of the deposition zone in order to achieve a finer spatial gas distribution and to mix the gases more evenly. The setup was also modified to let NH_3 enter the reactor with the bulk flow where it previously was channeled separately from the bulk flow to the deposition zone. Al_2O_3(001) substrates were selected as they provide a well-defined, inert surface, an easily characterized XRD pattern. This choice evades the additional chemical reactivity that, for instance, silicon substrates would induce. The substrates were used as received from MTI Corporation without any additional cleaning. A reduced flow of Ar was used for removing outgassing species during the heating of the reactor. A flow of 400 SCCM H_2 through the system for 5 min was applied to remove any previous halide remnants. Experiments were carried out using both stoichiometric equivalents of WF_6 to NH_3 to excessive amounts of ammonia (NH_3:$WF_6 = 25$).

A. LPCVD synthesis

The flow rates were controlled by separate mass flow controllers from MKS where WF_6 (99.88% purity from Alfax) and NH_3 (3.6 N purity from AGA Gas AB) were kept in separate internal channels and mixed only in the hot deposition zone. These measures were taken to avoid homogeneous adduct formation and deposition on the reactor walls in the preheated zone. The separation of gases also ensured that the gas mixture was not depleted at the substrate position, located 1 cm downstream from the shower head. The deposition times were kept long enough to pass the initial nucleation stage and enter into the growth stage. Still, the times were being kept short enough to keep the coating below 2 μm, allowing thickness measurements using XRF. The total pressure during deposition was kept at 1 Torr by using an automated butterfly valve and Ar balance (5.6 N purity). The total volumetric flow rate was fixed at 350 SCCM, which set the linear gas flow velocity at ∼3 m/s. The temperature was controlled by thermocouples located outside but close to the reactor wall. The recorded internal deposition temperature was calculated from a premeasured calibration curve.[12] Two main experimental series with fixed partial pressures were conducted to investigate the temperature dependence. The first set, A–F, from now on called "excess ammonia" or "100:4," used 100 SCCM NH_3 and 4 SCCM WF_6. The second series, G–J, called "stoichiometric" or "4:4," used flows of 4 SCCM NH_3 and 4 SCCM WF_6. To investigate the dependence of partial pressures, p_{NH_3} and p_{WF_6}, additional experiments were conducted, K–S, branching out from the two main series at 740 K. A summary of the experimental parameters is found in Table I.

© Author(s) 2021

TABLE I. Sample matrix describing the deposition temperature (T_{dep}), the deposition time (t_{dep}), and partial pressures of ammonia and tungsten hexafluoride (p_{NH_3} and p_{WF_6}). Experiments were carried out at 1 Torr with a total flow rate of 350 SCCM using Ar as balance. The linear flow rate over the substrate was estimated to ~3 m/s.

Sample	T_{dep} (K)	t_{dep} (s)	p_{WF_6} (Torr)	p_{NH_3} (Torr)
A	592	1500	0.011	0.286
B	641	1200	0.011	0.286
C	690	360	0.011	0.286
D	740	300	0.011	0.286
E	789	270	0.011	0.286
F	887	180	0.011	0.286
G	740	900	0.011	0.011
H	823	900	0.011	0.011
I	838	900	0.011	0.011
J	887	900	0.011	0.011
K	740	240	0.011	0.286
L	823	360	0.011	0.286
M	838	195	0.011	0.286
N	887	600	0.011	0.286
O	740	900	0.011	0.057
P	887	600	0.011	0.057
Q	740	900	0.003	0.011
R	740	900	0.023	0.011
S	887	900	0.023	0.011

B. Material characterization

Ion beam techniques are well-established, standard-free techniques that do not significantly alter the sample with regard to crystal structure. TOF-ERDA is sensitive to elements with low atomic number and, therefore, gives an opportunity to measure hydrogen concentrations and was employed to determine the composition of the coatings. The experiments were performed with a 36 MeV $^{127}I^{+8}$ beam, incident at 67.5° to the surface normal and with a recoil angle of 45°. The TOF-ERDA detector consists of a time-of-flight telescope followed by a gas ionization chamber so that both energy and time-of-flight of recoiled particles are recorded. Depth profiles were obtained with the software POTKU and CONTES. The composition was then determined from the bulk of the film where the concentrations converged.

XRD was performed on the samples using two D5000-systems from Siemens with a CuKα source (1.5418 Å). θ/2θ-data were collected using a standard Bragg–Brentano geometry with motorized divergence and antiscatter slits at 0.15° and 1°, respectively, and a 0.2 mm receiving slit. A curved graphite monochromator was equipped with a 1 mm detector slit.

Scanning electron microscopy (SEM) was employed for the investigations of the surface morphologies and cross sections of the coatings, using a Zeiss 1530 instrument equipped with a Schottky field emission gun (FEG) source. In-lens secondary electron images were acquired using an acceleration voltage of 2 kV and a working distance of ~4.7 mm.

Transmission electron microscopy (TEM) lift-out cross-section samples of the CVD films were prepared by the focused ion beam (FIB) method using an FEI Versa3D FIB-SEM instrument. Scanning transmission electron microscopy (STEM/TEM) analysis was done using an FEI Titan 80–300 TEM/STEM instrument operated at 300 kV. Transmission Kikuchi diffraction (TKD) measurements were performed using a Tescan GAIA3 FIB-SEM instrument using an Oxford NanoNordlys detector with an electron beam of 1.5 nA current accelerated at 20 kV.

C. Monitoring the LPCVD kinetics

Kinetics and growth rates of the CVD process, from film thickness measurements, were obtained by means of XRF using an Epsilon 3 instrument from PANalytical. The fluorescence yield was measured using a 1 mm thick Cu-mask on Teflon with a Ø 4 mm hole to keep the illuminated area constant. For tungsten analysis, $WL\beta_{1,2}$ peaks were chosen since the $WL\alpha_{1,2}$ contributions overlap the $CuK\alpha_{1,2}$ and $CuK\beta_1$ signals from the Cu-mask. The sum of the $WL\beta_{1,2}$ intensities was calculated by integrating these two overlapping peaks. The integrated intensities, corresponding to the density of W-atoms per unit area, are correlated with the thickness, h, via a calibration function of the form $F(h) = c(1 - e^{-a \cdot h})$. The constants, c and a, were calculated from measurements of a series of sputtered tungsten coatings with known thicknesses while the maximum yield limit was acquired from a sintered bulk W-sample. The fluorescence intensities of the CVD samples were well below the intensity observed for the bulk sample, ascertaining the validity of the method. The relative growth rates, R, were calculated by normalizing the intensities with respect to the deposition time. An Arrhenius plot (ln R vs 1/T) was applied to determine the apparent activation energy (AAE) and from that to deduce whether the process is controlled by mass transport or surface kinetics. Log-log plots (log R vs log p) were used for determining the partial reaction order, α and β, with respect to the individual partial pressures, p_{WF_6} and p_{NH_3}. From these parameters, the reaction rate is expressed as $R = A \times \exp(-AAE/RT) \times p_{WF_6}^{\alpha} \times p_{NH_3}^{\beta}$, where A is a pre-exponential constant.

III. RESULTS AND DISCUSSION

A. Elemental composition

TOF-ERDA was used for quantitative analysis of the elemental composition for some selected samples. The amount of W present in the coatings was constant, ~33–37 at. %, and appeared independent of temperature and the partial pressures of WF_6 and NH_3. However, some trends were observed in regard to the contents of N, O, F, and H present in the coatings. On changing the deposition temperature from 592 to 641 K, the amount of N increased to a stable level while instead reducing the F and H contents within the coatings. The ratio N:W was generally 1.6–1.8 for deposition temperatures of 641 K and above during excess conditions, with stoichiometric conditions being slightly lower, 1.5–1.6. At elevated partial pressure of NH_3, the concentration of N within the coating increased, while the opposite trend was true for F and O. This behavior is illustrated in Fig. 1. Some minor signals designated to Fe (~0.5 at. %) and Si or Al (0.5 at. %) were observed (not shown) in sample C deposited at 690 K. As for the origin of the signals of Al and Si, it emanates from either the substrate, contaminants in

© Author(s) 2021

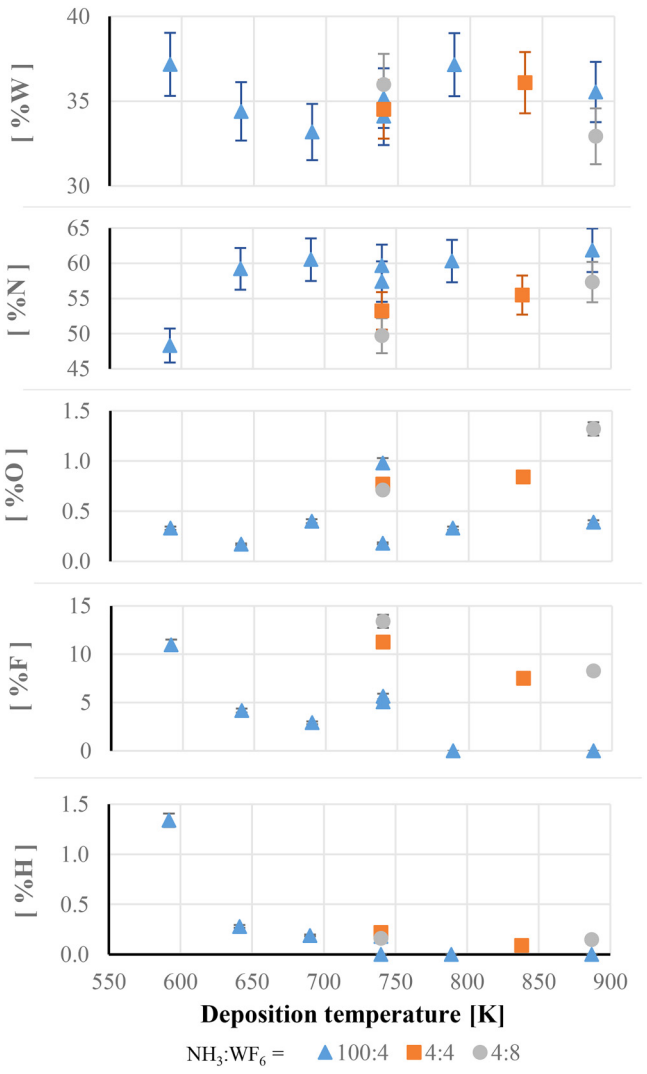

FIG. 1. ERDA compositional (at. %) analysis of the W, N, O, F, and H content for selected samples with different gas phase compositions; NH_3:WF_6 = 100:4 (A– K), 4:4 (G, J), and 4:8 (R, S).

the coating or the aluminum sample holder used. The values are low and they do not contribute significantly to influence the main conclusions of the kinetics in this paper.

Since the nitrogen concentration increased from 47% to 58% when increasing the temperature from 592 to 641 K, it indicates that there is an activation threshold in the NH_3 decomposition mechanism. At low temperatures (592 K), H and F levels were elevated. At this temperature, the system can be limited by either decomposition and/or desorption rates. In the first case, only partially decomposed NH_3 can react on the surface and this carries with it hydrogen impurities. Also, the amount of released H_2 from the decomposition reaction is reduced. Less H_2 in the system and a low reactivity from surface dwelling NH_3 subspecies cannot adequately reduce the incoming stream of WF_6 species to the growing surface. This means that the observed H can be assumed to be bonded to N while F remains bonded to W. This case is supported by studies where the ammonia decomposition over various catalytic surfaces has been made. In the work by Tamaru,[13] it can be seen that the trend for the decomposition rate is several orders of magnitude lower at T < 600 K and does not depend on either p_{NH_3} or p_{H_2}. Mukherjee *et al.*[14] presented the conversion for the decomposition process for several different materials. While the conversion approaches unity around ~800 K for some unique cases, at 592 K any conversion appears negligible for any of the materials presented. In the second case, a limit on the desorption rate of the HF by-product would also trap H and F in the material as the coating grows. The increase of the N content (above 650 K) is expected as the conversion of NH_3(g) would increase with temperature and so would the partial surface coverage of adsorbed/chemisorbed N containing species. Also, it was observed that the amount of incorporated F was reduced. This is also expected since an increase of adsorbed NH_3 subspecies would shift the equilibrium toward further product formation, leading to HF as a by-product that after desorption is pumped out of the system. The level of O in the coatings is low and is assumed to be partly caused by the exposure to air postdeposition forming oxyfluorides. However, it was observed that coatings formed under the condition of excess ammonia contained less O. This is likely linked to fluorine, which can form HF with the H_2O in the environment postdeposition. It is seen that the samples with the higher F content are also exhibiting more O. This is not the case for the sample deposited at 592 K; however, this sample is amorphous, as is shown in Sec. III B, and the amount of diffusion pathways is reduced which stops the air from contaminating the sample.

B. Phase composition

XRD was used to identify the phase content of the samples. For all these samples, the θ/2θ diffraction data in the out-of-plane direction were acquired in the 30°–150° range. The coatings deposited up to 641 K were x-ray amorphous. At higher deposition temperatures, β-W_2N (PDF 025-1257, a = 4.12 Å) was identified but with a larger cell parameter, ~4.165 Å. The strongest peaks were those of the (111) planes as well as the peaks of (200), (311), (331), (420), and (422) being observable; however, at a significantly lower magnitude. Two peaks were identified as the (000l) of the α-Al_2O_3 substrate. One peak remained unidentified. θ/2θ-data for selected samples deposited at stoichiometric and excess conditions at 592, 740, 789, and 887 K are shown in Fig. 2.

At 592 and 641 K, the deposited material appeared amorphous with only a single, broad peak at 2θ = 36°. No further features other than the sharp peaks expected from the α-Al_2O_3 substrate were observed. As the deposition temperature reached 690 K, crystallinity was emerging and a diffraction pattern that could be fitted to β-W_2N. This structure can be described as a ccp substructure of W-atoms with N randomly filling octahedral holes at first but then also tetrahedral holes as *x* increases. The expected increase in cell volume can be explained by the high N content observed by ERDA. The cell parameter in the out-of-plane direction was

© Author(s) 2021

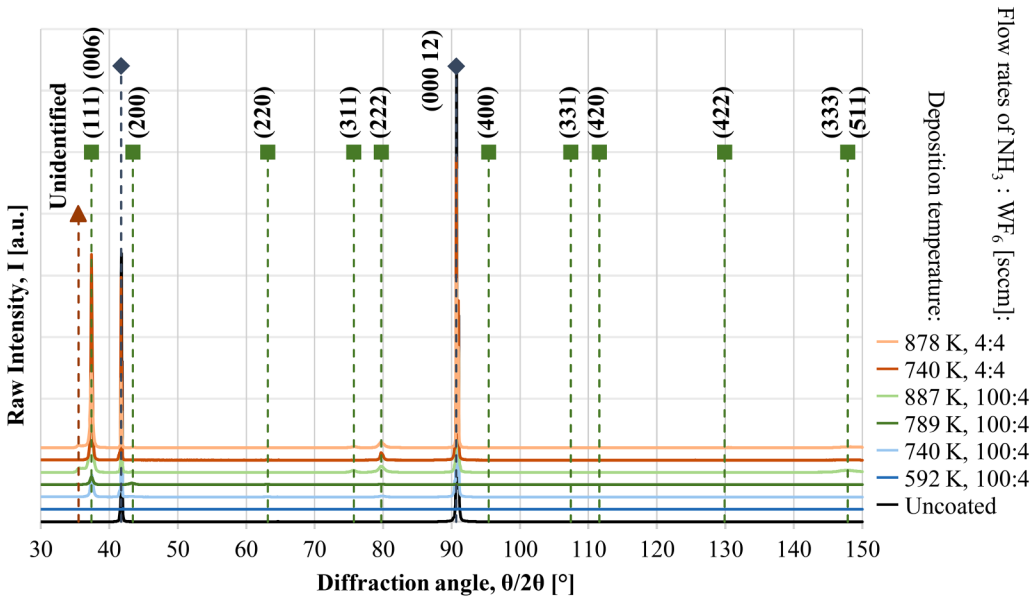

FIG. 2. Out-of-plane diffraction raw data of different deposition temperatures and gas compositions. Samples in ascending order: uncoated substrate, A, D, E, F, G, and J. Substrate data added for reference. Peaks correspond to ■ β-W_2N (a = 4.165 Å), ◆ α-Al_2O_3, and ● an unidentified peak.

generally in the range of a = 4.16–4.17 Å, with a small dependence on T and p_{NH_3}. The material deposited at 690 K also showed some additional peaks that were most likely originating from fluorides of iron and aluminum as was indicated by TOF-ERDA. Again, the amount of contaminants is very low and should not influence the conclusions with regard to kinetics to a significant degree. At a deposition temperature of 740 K, an unidentified peak appeared in some samples. The peak adds a clear shoulder on the left side of the β-W_2N (111) peak and could belong to either β-W or h-WN. Some asymmetrical broadening of the other β-W_2N peaks supports the presence of β-W. However, subsequent TEM analysis found no evidence of the existence of either of these two phases. Contributions from tungsten containing impurities that overlap those of β-W_2N make it demanding to determine the exact distribution of W between the different phases. The magnitude of the possible overlapping peaks from the other phase is significantly weaker compared to the most intense coating peak, i.e., β-W_2N (111). It is reasonable to assume that the amount of the contaminating phase is very low. XRD of β-W_2N by Nagai *et al.*[15] appears to contain a similar phase when deposited at 1063 K, although no description of this peak is given.

The texture coefficient (TC)[16,17] was used as a simple indicating parameter for the coating texture. TC was calculated under the assumption that the sample consists of pure β-W_2N. Thin film absorption correction was applied to compensate for thickness variations, although yielded little difference due to the sample thicknesses. Relative powder intensities were simulated using CARINE 3.1 software using PDF 025-1257 as reference. From that analysis, the samples appear to be dominated by the <111> growth direction, but <100> also appears strongly in some samples, however, lacking an obvious temperature dependence. The calculated TC is seen in Table II.

TEM was used to produce selected area electron diffraction (SAED) patterns from the samples deposited with excess ammonia at 592, 740, 789, and 887 K. The acquired SAED patterns showed that there was a gradual transition in structural order of the coatings as the deposition temperature was increased, from amorphousness to finely grained polycrystallinity and, eventually, to pronounced grain growth. The recorded diffraction patterns are presented in Fig. 3.

These results confirmed the XRD results also on a micrometer scale. At 592 K, the sample diffraction feature comes out as a fuzzy ring, see Fig. 3(a). The sample deposited at 740 K, while morphologically similar to that deposited at 592 K, is polycrystalline as

TABLE II. Calculated TC values of WN_x coatings on (00l) α-Al_2O_3 at different deposition temperatures and molar flow ratios of WF_6 and NH_3.

Sample	D	E	F	G	J
NH_3:WF_6	100:4	100:4	100:4	4:4	4:4
T_{dep} (K)	740	789	887	740	887
T_C					
(1 1 1)	6.12	3.51	5.72	6.97	5.88
(0 0 2)	0.28	1.20	0.04	0.01	0.04
(2 2 0)	0.19	0.70	0.04	0.01	0.07
(3 1 1)	0.11	0.47	0.77	0.00	0.51
(3 3 1)	0.08	0.36	0.03	0.00	0.03
(4 2 0)	0.07	0.34	0.05	0.00	0.05
(4 2 2)	0.15	0.43	0.35	0.01	0.42

© Author(s) 2021

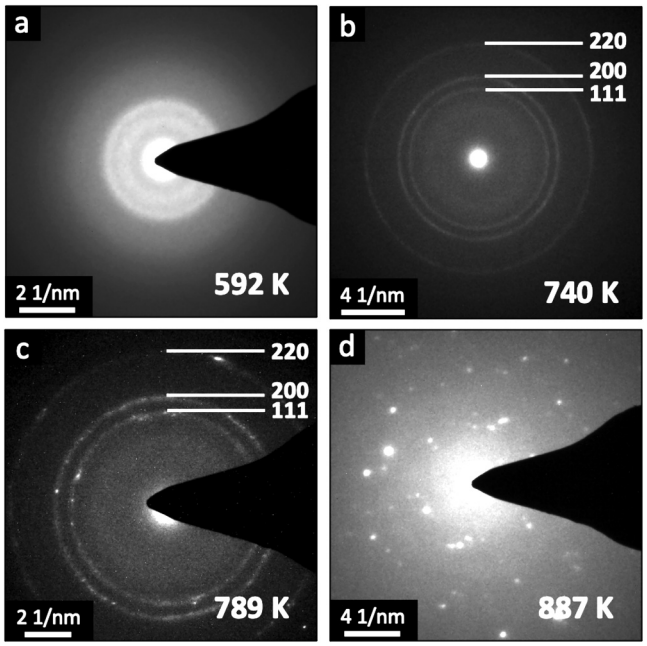

FIG. 3. TEM SAED patterns from samples A, D, E, and F deposited using excess ammonia at (a) 592, (b) 740, (c) 789, and (d) 887 K, respectively.

indicated by the rings in Fig. 3(b). At 789 K, Fig. 3(c), the diffraction pattern shows features of polycrystalline rings with occasional spots from larger grains. The 887 K sample, Fig. 3(d), also displayed polycrystallinity. The grains in this sample are larger, and the continuous rings seen previously have turned into a discrete number of diffraction spots. This is due to the limited amount of analyzed grains within the FIB-lamella.

C. Morphologies and microstructures

A stark difference in morphology was observed between samples deposited using excess ammonia and those deposited using stoichiometric amounts. At deposition temperatures below 740 K, the surface contained nodular surface features. At higher deposition, temperatures facetted crystals started to emerge. Top surface SEM micrographs of the coatings deposited using excess ammonia at 592, 740, 789, and 887 K can be seen in Figs. 4(a)–4(d). Those deposited with stoichiometric amounts of ammonia at 740 and 887 K can be seen in Figs. 4(e) and 4(f). Cross sections from TEM of the coatings deposited with excess ammonia as mentioned are seen in Fig. 5.

The transition from amorphous to crystalline growth, shown by XRD in the range 641–690 K, is not clearly obvious from the observed morphology of the samples, Figs. 4(a) and 4(b). The amorphous samples appear as nodular with a weak contrast, Fig. 4(a), while the crystalline sample deposited at 740 K appeared featureless. The microstructures of these samples, Figs. 5(a) and 5(b), were also featureless. The exception is the amorphous sample having convex curvatures at the top surface with a width of ~200 nm, which is the approximate size of the nodes seen in Fig. 4(a). At a deposition of 740 K using stoichiometric amounts NH_3, the surface morphology still showed nodular features with a weak contrast, see Fig. 4(e), similar to those seen for the amorphous sample but smaller in size.

At a deposition temperature of 789 K using excess ammonia, see Fig. 4(c), it was observed that most of the otherwise fine-grained surface was sparsely occupied by larger facetted grains. This is concordant with the conclusion by Nagai *et al.*[15] that the transition temperature between the amorphous and crystalline

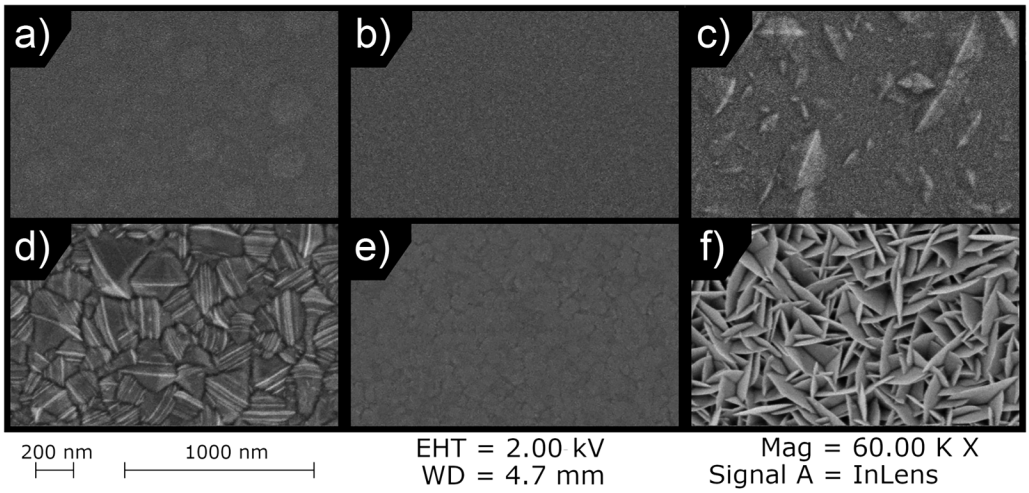

FIG. 4. Top surface SEM images of samples A, D, E, and F deposited using excess ammonia at (a) 592, (b) 740, (c) 789, (d) 887 K, and samples G and J deposited using stoichiometric parts ammonia and hexafluoride at (e) 740 and (f) 887 K.

© Author(s) 2021

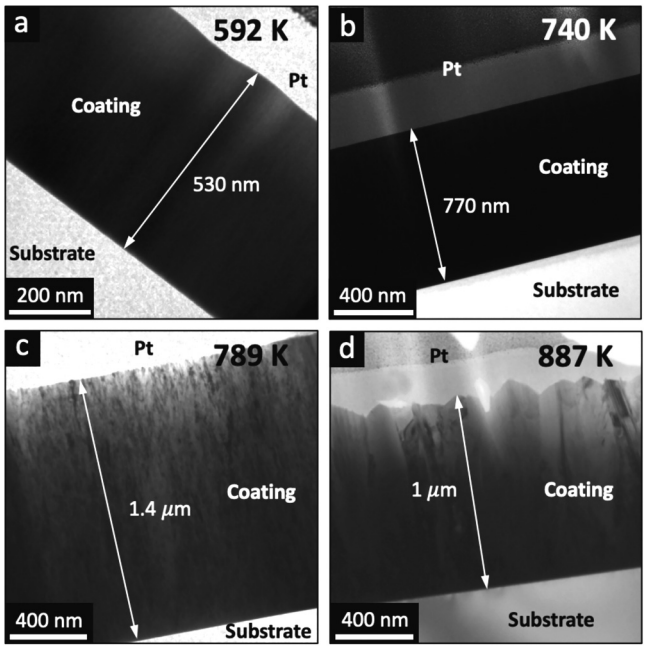

FIG. 5. TEM BF micrographs from sample coatings A, D, E, and F deposited using excess ammonia at different deposition temperatures. (a) 592, (b) 740, (c) 789, and (d) 887 K, respectively.

mode of growth using WF_6 is at around 789 K. This can also be seen in Fig. 5(c), where a crystalline phase is observed at this temperature. At 887 K, larger columnar grains have evolved. However, the observations made here by XRD indicate that crystallinity can emerge at lower temperatures, i.e., ~690 K. This difference in results is believed to be due to the reactor setup with regard to preheating and premixing of gases. In the TEM cross-section micrographs, see Fig. 5(c), it was observed that the sample contained a large amount of defects. The change in morphology observed for the deposition at 789 K has two likely explanations: competitive growth and/or twinning. First, for competitive growth, nucleation of small crystals typically occurs at the substrate-coating interface.[18,19] Then, one or two of the fastest growing orientations will outpace the others and eventually grow to dominate the film. Second, considering twinning, a well textured film has only one growth direction and a limited growth rate. If then, a stacking fault/twinning event occurs that creates a faster growing crystallographic orientation in the out-of-plane direction, that fault will grow, creating a protrusion.[20]

At a deposition temperature of 887 K, the coatings consist of larger columnar crystals, see Figs. 4(d), 4(f), and 5(d). The sample produced when using stoichiometric ratios shows large disc-shaped protrusions occupying the surface, see Fig. 4(f). This latter morphology resembles that of <211>-oriented TiN (Ref. 17) under certain deposition conditions.

In contrast, the grains deposited when using excess ammonia showed facets covered by ridgelike protrusions, giving the grains a lamellar appearance. The TEM micrographs showed that these protrusions were aligned in the out-of-plane direction. This is obvious from the left most grain in Fig. 5(d) and may be the subject of a later study. It also is seen that the film is very fine grained close to the substrate/coating interface. Continuous nucleation appears to be the primary mode of the growth for the first 300 nm or so. After that, a change of microstructure to produce larger, wedge-shaped grains occur. This is typical for competitive growth as explained earlier. Transmission Kikuchi diffraction was used to produce inverse pole figures (IPFs) and pole figures (PFs) for determining the texture of the coating, Fig. 6.

The dominating texture was in the <211> direction as indicated by the concentrated intensity from the IPF seen in Fig. 6(b). From an analysis of the pole figures, Fig. 6(c), it is concluded that the <211> direction is aligned with the surface normal direction Y while <111> is not. This apparently disagrees with the TC calculation made previously. As pointed out, a correct evaluation of the texture by that indicator requires a good determination of the intensities from the β-W_2N phase, which here suffer from overlap by contributions from other phases at the <422> position. However, the entire coating contributes to the observed XRD intensities. TEM analyses a significantly reduced sample size of crystals, and local biases can thus arise. In this case, Kikuchi diffraction requires sufficiently large crystals for a determination of their orientation. The sampled grains can be seen in Fig. 6(a). The coating at the interface is too fine grained and does not contribute to the collected data. The <211> texture from Kikuchi diffraction is more localized to the surface while the <111> texture as deduced from the TC analysis can be attributed to the part closer to the substrate interface. This appears analogous to the CVD-Ti(C,N) system where the texture tends to switch from Ti(C,N)(111)|| α-Al_2O_3(0001) to a <211> orientation as the coating thickness increases.[20] At first, substrate interaction is dominating in determining the orientation of the coating. At a certain coating thickness, the influence of the substrate has diminished enough to allow for a process-controlled deposition mechanism.

D. LPCVD kinetics

The growth kinetics of CVD-WN_x was investigated by plotting the relative growth rate, R, as a function of temperature and partial pressures. The average growth rate may be obtained when the coating thickness is normalized with regard to the total deposition time. While this approach is simple it has drawbacks as variations in homogeneity and coating density might cause the direct relationship between thickness and reaction rate to deviate between samples. By using XRF, the mass absorption is measured that circumvents the issue arising from possible density variations. In this way, the number of atoms, in this case W, found within the probed volume can be correlated to the coating thickness. The selected XRF peak, here W$L\beta_{1,2}$, was integrated and the intensity was normalized to yield an average growth rate. From the calculated growth rates, ln R was plotted as a function of reciprocal deposition temperature, 1/T, yielding an Arrhenius plot, see Fig. 7. From regression analysis of the Arrhenius plot, an estimate of the apparent activation energy (AAE) of the process at a given deposition temperature can be achieved from the slope at that point. This was done employing a linear fit for both gas mixture compositions,

© Author(s) 2021

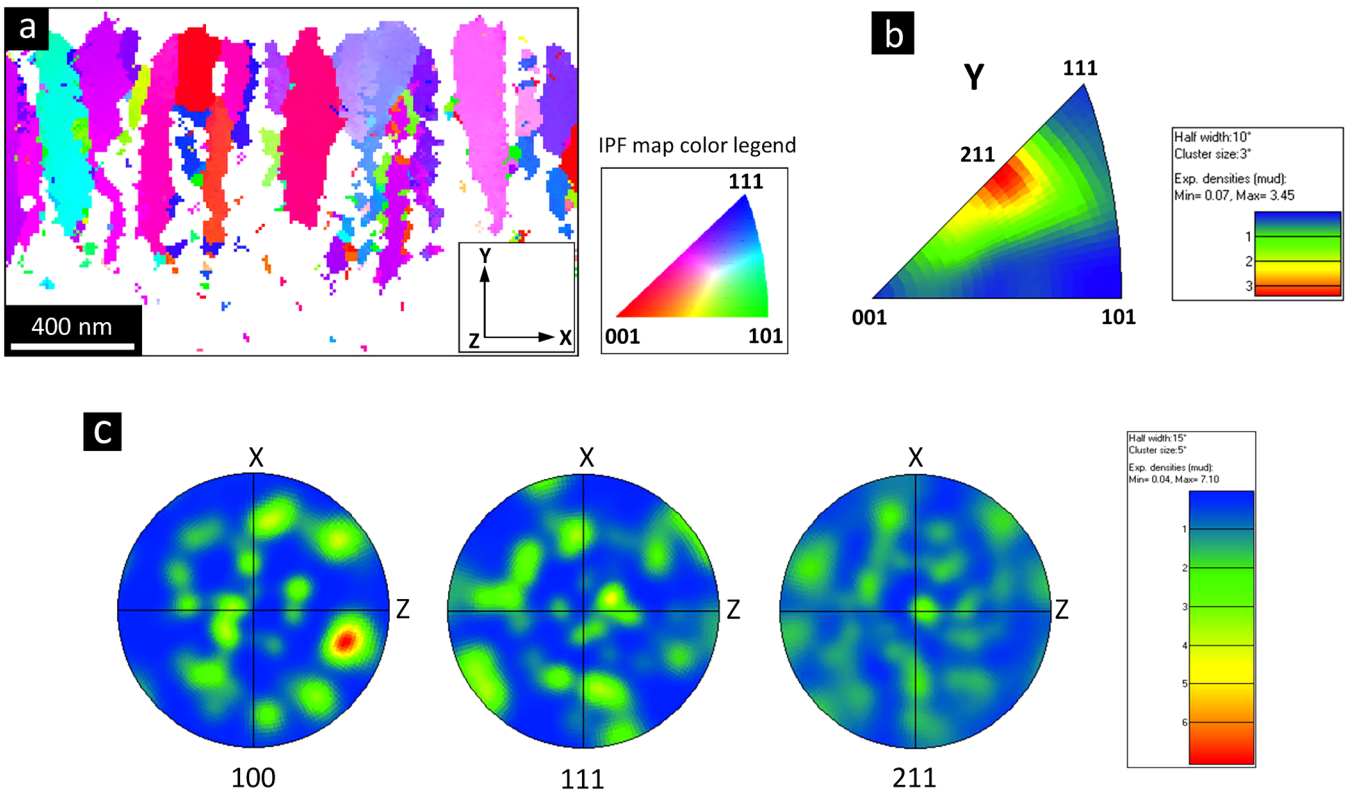

FIG. 6. TKD results of sample F deposited at 887 K employing excess ammonia. (a) IPF map of the sampled grains along the coating growth (Y) direction. (b) IPFs along the Y direction. (c) Pole figures of the 100, 111, and 211 poles.

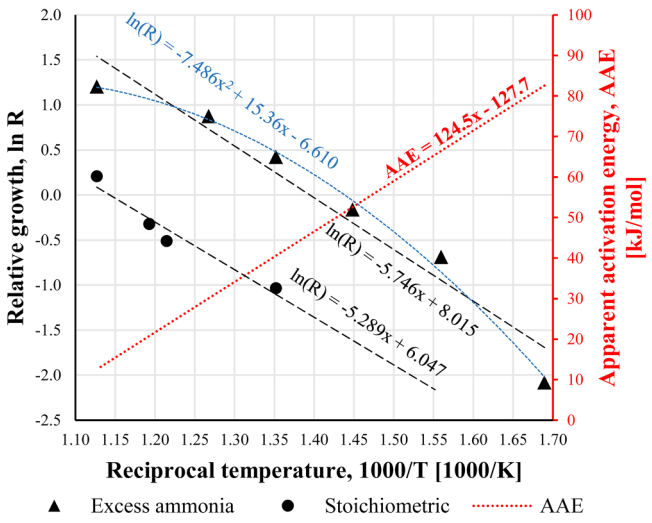

FIG. 7. Arrhenius plot using XRF data—ln R vs 1/T using excess ammonia (samples A–F) and equal parts NH_3 and WF_6 (samples G–J). Apparent activation energy plotted from the quadratic fit of the excess ammonia data.

those with excess and stoichiometric amounts of ammonia, yielding values of 48 and 44 kJ/mol, respectively. For the excess ammonia, a quadratic fit was made where the estimated AAE as a function of temperature is plotted on the right axis in red. The activation energy ranged between 12 and 82 kJ/mol within the investigated deposition temperature range.

From the XRD diffractogram, Fig. 2, it can be seen that the amorphous growth dominated up to 641 K after which a crystalline β-W_2N phase emerged at 690 K. This phase then dominated for deposition temperatures of 740–887 K. Considering rate kinetics, the values for the AAE in a mass transport/diffusion-controlled process typically lie in the range of 15–20 kJ/mol, while values mostly exceed 40 kJ/mol when the chemical system is surface-reaction limited, and then often in the range of 100–400 kJ/mol.[21–23]

The films deposited above 789 K thus seem to be governed by diffusion control, while other samples are most likely a result of mixed contributions, Fig. 7. Nagai *et al.*[24] explored the WF_6-NH_3-H_2-Ar system and obtained an AAE of 62 kJ/mol in the range of 592–690 K. The value obtained here using the quadratic fit at 641 K is 72 kJ/mol is attributed to the difference in deposition conditions compared to Nagai *et al.*

Log-log plots for different deposition temperatures were constructed as log R versus $\log p_{NH_3}$ and $\log p_{WF_6}$, respectively, see

© Author(s) 2021

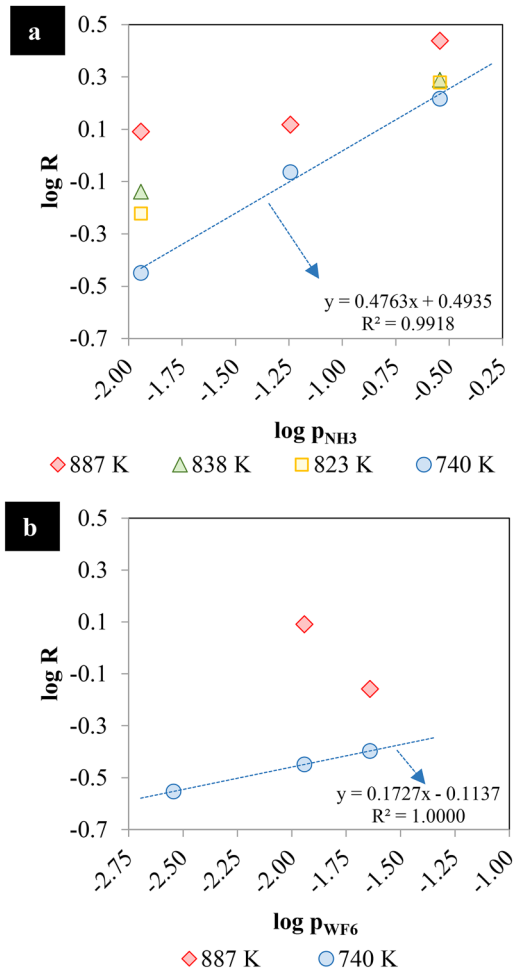

FIG. 8. Effect on the growth rate by (a) p_{NH_3} keeping p_{WF_6} fixed at 0.01 Torr (samples G–P) and (b) p_{WF_6} keeping p_{NH_3} fixed at 0.01 Torr (samples G, J, and Q–S). Linear regression is given for the case of a deposition temperature of 740 K with three sample points.

Fig. 8. The log-log plot gives information regarding the magnitude of the influence of the gas partial pressure on the growth rate. From the tangent of the curve, the partial reaction order can be deduced. A linear fit is given at 740 K as this temperature is expected to be the most kinetically limited.

It can be seen in Fig. 8(a) that the ammonia has a low but positive effect on the growth rate with the slope indicating a partial reaction order of ~0.5 at 740, 823, and 838 K. This is close to the value of 0.65 obtained by Nagai *et al.*[24] at 789 K. At 887 K, this trend also appears to be true when the partial pressure of ammonia is high. Initially, the increase in R is minuscule as the partial pressure increases from ~0.01 to 0.06 Torr, ammonia appears to have little or no influence on the growth rate. This is interpreted as a mass transport limitation. Once a sufficient quantity of ammonia reaches the sample surface, kinetics will start to limit the reaction rate. The value obtained here is comparable to the partial reaction order of H_2 in the CVD-W process from WF_6 and H_2, which is reportedly 1/2.[24,25]

The influence of p_{WF_6}, seen in Fig. 8(b), is low at 740 K with an obtained value of 0.17 for the partial reaction order. Nagai *et al.*[24] did obtain a value of 0.5 and 1 when depositing at 690 and 789 K, respectively, in their study which included H_2 in the process at slightly different deposition conditions. The value obtained here can be compared to the reported value in the CVD-W process using H_2 where the partial reaction order for that process with respect to p_{WF_6} was reported as 0 by Broadbent *et al.*[25] At similar deposition conditions, Bryant[26] reported 1/6 at slightly higher temperature and pressure. At a deposition temperature of 887 K, the slope was found to be negative. This is interpreted as a sign of gas phase depletion as was previously seen in the Arrhenius plot, Fig. 7. The conclusion is a rate expression of $R = A \times \exp(-46\ \text{kJ/mol/RT}) \times p_{WF_6}^{1/6} \times p_{NH_3}^{1/2}$ using the average AAE for the two investigated gas compositions.

IV. CONCLUSIONS

Cubic WN_x films were deposited on single crystal Al_2O_3 (000l) substrates in a deposition temperature range of 592–887 K.

- The elemental compositions were similar at deposition temperatures of 641 K and higher, with an N:W ratio of 1.65 with no obvious dependence on T, p_{WF_6}, or p_{NH_3}.
- Films were amorphous at deposition temperatures below 690 K. Films crystallized in the β-W_2N structure above this limit.
- A minor content of an unidentified phase was also deposited using excess ammonia at a deposition temperature of 740 K. Using stoichiometric amounts of NH_3 and WF_6, this phase was not observed at this temperature.
- Films appeared smooth in SEM from the amorphous material deposited at 592 K to the β-W_2N deposited at 740 K. At a deposition temperature of 789 K larger crystal facets were protruding the otherwise smooth surface.
- The morphology changed at a deposition temperature of 550 K for excess ammonia, with crystal facets featuring ridgelike protrusions and a lamellar appearance in SEM. Texture determination via XRD TC showed a dominating <111> out-of-plane direction in the crystalline samples. TKD showed that the major part of the deposited material was oriented with the <211> direction aligned with the surface normal. On using stoichiometric amounts NH_3 and WF_6, the sample coating deposited at 887 K displayed protruding disc-shaped crystals. This morphology is similar to that of <211> textured TiN.
- The microstructure evolution as a function of temperature is typical for a CVD deposited coating. As temperature increases, the grain size increases. At the highest deposition temperature (887 K), the grains are columnar.
- From linear regression, excess ammonia and stoichiometric conditions both yield similar activation energies, 48 and 44 kJ/mol respectively, averaging at 46 kJ/mol. As deduced from a quadratic fit for the excess ammonia data, the apparent activation energy ranged from 82 kJ/mol at 592 K to 12 kJ/mol at 887 K.
- At a deposition temperature of 740 K, the partial reaction order with respect to NH_3 was estimated to ~1/2 with respect to NH_3.

© Author(s) 2021

This trend was maintained up to 838 K. As the deposition temperature reached 887 K, the trend appeared to be maintained at higher ammonia partial pressures while leveling off as the partial pressure is reduced ($p_{NH_3} = 0.01$).

- The partial reaction order was estimated to ~1/6 with respect to WF_6 at a deposition temperature of 740 K. At a deposition temperature of 887 K, the reaction order was negative that was interpreted as the same mass transport limitation of NH_3 discussed earlier but amplified due to the increased amount of WF_6 in the gas phase.
- The average rate expression was evaluated as

$$R = A \times p_{WF6}^{1/6} \times p_{NH3}^{1/2} \times \exp(-46\,\text{kJ/mol/RT}).$$

ACKNOWLEDGMENTS

The funding of CVD 2.0 by the Swedish Foundation for Strategic Research via SSF Contract No. RMA15-0048 is gratefully acknowledged. Fundings from Sandvik AB and the Inorganic Chemistry programme at Chemistry Ångström, Uppsala University are gratefully acknowledged as well. The TEM experiments were carried out at the Chalmers Materials Analysis Lab (CMAL). The ERDA measurements were conducted at the Tandem Laboratory at Uppsala University.

CONFLICT OF INTEREST

There are at the time of submission no conflicts of interest.

DATA AVAILABILITY

The data that support the findings of this study are available within the article or from the corresponding author upon reasonable request.

REFERENCES

[1]L. Ulmer, L. Georges, J. C. Veler, Y. Morand, M. Bakli, V. Ferrier, M. Lerme, L. Perroud, and T. Morel, Microelectron. Eng. **33**, 121 (1997).
[2]N. Gonohe, Mater. Trans. **43**, 1585 (2002).
[3]P. J. Van Der Put, J. A. M. Ammerlaan, J.-P. Dekker, and J. Schoonman, Chem. Vap. Depos. **5**, 211 (1999).
[4]J. W. Klaus, S. J. Ferro, and S. M. George, Appl. Surf. Sci. **162–163**, 479 (2000).
[5]Y. H. Hwang, W. J. Cho, and Y. Kim, Jpn. J. Appl. Phys. **52**, 10MC07 (2013).
[6]A. Kafizas, C. J. Carmalt, and I. P. Parkin, Coord. Chem. Rev. **257**, 2073 (2013).
[7]T. Nakajima, K. Watanabe, and N. Watanabe, J. Electrochem. Soc. **134**, 3175 (1987).
[8]W. Frankenburger and A. Hodler, Trans. Faraday Soc. **28**, 229 (1932).
[9]See https://cameochemicals.noaa.gov/chemical/2427 for "Cameo Chemicals: Ammonium Fluoride" (last accessed March 1, 2021).
[10]D. Lide, *CRC Handbook of Chemistry and Physics*, 86th ed. (CRC, Boca Raton, 2005).
[11]H. C. Clark and H. J. Emeléus, J. Chem. Soc. **1957**, 4778.
[12]J. G. Hulkko, *Muspel and Surtr: CVD System and Control Program for WF_6 Chemistry* (Uppsala University, Uppsala, Sweden, 2019).
[13]K. Tamaru, Acc. Chem. Res. **21**, 88 (1988).
[14]S. Mukherjee, S. V. Devaguptapu, A. Sviripa, C. R. F. Lund, and G. Wu, Appl. Catal. B: Environ. **226**, 162 (2018).
[15]M. Nagai and H. Nakaya, Mater. Sci. Forum **554**, 65 (2007).
[16]A. Larsson and S. Ruppi, Thin Solid Films **402**, 203 (2002).
[17]H.-E. Cheng and M.-H. Hon, J. Appl. Phys. **79**, 8047 (1996).
[18]I. Petrov, P. B. Barna, L. Hultman, and J. E. Greene, J. Vac. Sci. Technol. A **21**, S117 (2003).
[19]J. A. Thornton, Annu. Rev. Mater. Sci. **7**, 239 (1977).
[20]L. von Fieandt, K. Johansson, T. Larsson, M. Boman, and E. Lindahl, Thin Solid Films **645**, 19 (2018).
[21]H. S. Kong, J. T. Glass, and R. F. Davis, J. Mater. Res. **4**, 204 (1989).
[22]J.-O. Carlsson, J. Less Common Met. **71**, 1 (1980).
[23]C. H. L. Goodman, *Crystal Growth: Theory and Techniques* (Springer, Boston, MA, 1974).
[24]M. Nagai, K. Kishida, and S. Omi, Nippon Kagaku Kaishi **10**, 907 (1994) (in Japanese).
[25]E. K. Broadbent and C. L. Ramiller, J. Electrochem. Soc. **131**, 1427 (1984).
[26]W. A. Bryant and G. H. Meier, J. Electrochem. Soc. **120**, 559 (1973).

© Author(s) 2021